THE X-RAY PROPERTIES OF TYPICAL HIGH-REDSHIFT RADIO-LOUD QUASARS

Citation: Saez, C., W. N. Brandt, O. Shemmer, L. Chomiuk, L. A. Lopez, H. L. Marshall, B. P. Miller, and C. Vignali. "THE X-RAY PROPERTIES OF TYPICAL HIGH-REDSHIFT RADIO-LOUD QUASARS." The Astrophysical Journal 738, no. 1 (August 11, 2011): 53. © 2011 The American Astronomical Society

As Published: http://dx.doi.org/10.1088/0004-637x/738/1/53

Publisher: IOP Publishing

Persistent URL: http://hdl.handle.net/1721.1/95650

Version: Final published version: final published article, as it appeared in a journal, conference proceedings, or other formally published context

The Astrophysical Journal, 738:53 (12pp), 2011 September 1 doi:10.1088/0004-637X/738/1/53

THE X-RAY PROPERTIES OF TYPICAL HIGH-REDSHIFT RADIO-LOUD QUASARS

C. Saez[1], W. N. Brandt[1], O. Shemmer[2], L. Chomiuk[3,4], L. A. Lopez[5], H. L. Marshall[6], B. P. Miller[7], and C. Vignali[8,9]
[1] Department of Astronomy & Astrophysics, Pennsylvania State University, University Park, PA 16802, USA; saez@astro.psu.edu
[2] Department of Physics, University of North Texas, Denton, TX 76203, USA
[3] Jansky Fellow of the National Radio Astronomy Observatory, Charlottesville, VA 22903, USA
[4] Harvard-Smithsonian Center for Astrophysics, 60 Garden Street, Cambridge, MA 02138, USA
[5] Department of Astronomy and Astrophysics, University of California Santa Cruz, 159 Interdisciplinary Sciences Building, 1156 High Street, Santa Cruz, CA 95064, USA
[6] Kavli Institute for Astrophysics and Space Research, Massachusetts Institute of Technology, 77 Massachusetts Ave., Cambridge, MA 02139, USA
[7] Department of Astronomy, University of Michigan, 500 Church Street, Ann Arbor, MI 48109, USA
[8] Dipartimento di Astronomia, Università degli Studi di Bologna, Via Ranzani 1, 40127 Bologna, Italy
[9] INAF Osservatorio Astronomico di Bologna, Via Ranzani 1, 40127 Bologna, Italy
Received 2011 March 31; accepted 2011 June 12; published 2011 August 11

ABSTRACT

We report spectral, imaging, and variability results from four new *XMM-Newton* observations and two new *Chandra* observations of high-redshift ($z \gtrsim 4$) radio-loud quasars (RLQs). Our targets span lower, and more representative, values of radio loudness than those of past samples of high-redshift RLQs studied in the X-ray regime. Our spectral analyses show power-law X-ray continua with a mean photon index, $\langle\Gamma\rangle = 1.74 \pm 0.11$, that is consistent with measurements of lower redshift RLQs. These continua are likely dominated by jet-linked X-ray emission, and they follow the expected anticorrelation between photon index and radio loudness. We find no evidence of iron Kα emission lines or Compton-reflection continua. Our data also constrain intrinsic X-ray absorption in these RLQs. We find evidence for significant absorption ($N_{\rm H} \approx 1.7 \times 10^{22}{\rm cm}^{-2}$) in one RLQ of our sample (SDSS J0011+1446); the incidence of X-ray absorption in our sample appears plausibly consistent with that for high-redshift RLQs that have higher values of radio loudness. In the *Chandra* observation of PMN J2219−2719 we detect apparent extended (∼14 kpc) X-ray emission that is most likely due to a jet; the X-ray luminosity of this putative jet is ≈2% that of the core. The analysis of a 4.9 GHz Very Large Array image of PMN J2219−2719 reveals a structure that matches the X-ray extension found in this source. We also find evidence for long-term (450–460 days) X-ray variability by 80%–100% in two of our targets.

Key words: cosmology: observations – galaxies: active – X-rays: galaxies

Online-only material: color figures

1. INTRODUCTION

Active galactic nuclei (AGNs) are tracers of supermassive black hole (SMBH) growth in the centers of galaxies. This activity can be used to find and probe the evolution of massive galaxies at cosmological epochs close to the period of reionization (e.g., Fan et al. 2006). The study of high-redshift quasars ($z \gtrsim 4$) is particularly important because it provides information on the period when the first SMBHs were formed in the Universe. X-ray studies reveal conditions in the immediate vicinity of these SMBHs as well as their larger scale environment (e.g., with intrinsic or intervening absorption). Most X-ray studies of high-redshift quasars have focused on radio-quiet quasars (RQQs; those with radio-loudness[10] parameter $R_L \lesssim 10$). The main result of these studies is that high-redshift RQQs have similar X-ray properties (e.g., X-ray power-law photon index, Γ, and optical-to-X-ray power-law slope,[11] $\alpha_{\rm ox}$) to those at lower redshift ($z = 1$–3) of matched luminosity (e.g., Shemmer et al. 2006; Just et al. 2007).[12] Thus, high-redshift RQQs seem to be feeding and growing in a generally similar manner to those at lower redshift.

Radio-loud quasars (RLQs; those with $R_L \gtrsim 10$–100) have strong radio emission which is usually linked to the presence of jets emitted from the AGN at relativistic speeds (e.g., Begelman et al. 1984). X-ray spectral and variability studies of high-redshift RLQs provide a probe of their pc-scale jet-linked X-ray emission, since this jet-linked emission often dominates the observed X-ray luminosity. Due to this jet-linked component, RLQs have stronger X-ray emission than RQQs of similar optical/UV luminosities (e.g., Zamorani et al. 1981). This excess in X-ray emission increases with the radio loudness (e.g., Worrall et al. 1987); for example, for $\log R_L \sim 4$ the X-ray luminosity of RLQs can be up to ∼10 times higher than the luminosity of RQQs with similar optical/UV luminosity (e.g., Miller et al. 2011). The jet-linked emission of RLQs also makes their X-ray spectra harder as R_L increases (e.g., Wilkes & Elvis 1987; Reeves & Turner 2000). RLQs represent 10%–20% of the whole quasar population (e.g., Ivezić et al. 2002; Jiang et al. 2007). Notably, the frequency of radio jets in luminous quasars seems to change significantly with redshift and UV luminosity (e.g., Jiang et al. 2007). Thus, it is of interest to assess if the physical processes operating within jets also change with redshift; any such changes should probably be most apparent at the highest redshifts. RLQs at $z \gtrsim 4$ have been studied much less well in the X-ray regime than correspondingly high-redshift RQQs. The number of sensitive exploratory X-ray observations

[10] The radio-loudness parameter (R_L) is defined as the ratio between the flux density at 5 GHz and the flux density at 4400 Å in the rest frame of the source (Kellermann et al. 1989).
[11] The optical-to-X-ray power-law slope is defined as $\alpha_{\rm ox} = \log(f_{2\,\rm keV}/f_{2500\,\text{Å}})/\log(\nu_{2\,\rm keV}/\nu_{2500\,\text{Å}})$ (Tananbaum et al. 1979).
[12] For RQQs, $\alpha_{\rm ox}$ shows a dependence upon the UV luminosity (e.g., Steffen et al. 2006). For these sources there is also evidence that Γ may depend on the X-ray luminosity (e.g., Saez et al. 2008) and/or the accretion rate (in terms of the Eddington ratio; e.g., Shemmer et al. 2008).

(and thus X-ray detections) is much smaller (20–30 in total), and the number of RLQs with quality X-ray spectra is even smaller still ($\lesssim$10). Those $z \gtrsim 4$ RLQs that have been targeted for X-ray spectroscopy are usually highly radio loud ($R_L > 1000$; e.g., Worsley et al. 2004; Yuan et al. 2006). Such highly radio-loud objects make up only a small fraction ($\lesssim$5%) of the RLQ population, so they are not representative objects.

X-ray observations of high-redshift RLQs with good angular resolution can also facilitate study of kpc-scale X-ray jets. Two of the most popular models for this kpc-scale emission (e.g., Worrall 2009, and references therein) are (1) an extra high-energy synchrotron component and (2) inverse Compton (IC) scattering by relativistic electrons of photons of the cosmic microwave background (CMB; or the IC/CMB model). For synchrotron models, we do not obviously expect that the X-ray emission properties would depend on redshift. The energy density of the CMB increases as $(1+z)^4$; as a consequence, an implication of the IC/CMB model is that for high-redshift RLQs ($z \gtrsim 4$) the X-ray emission from extended jets may outshine that from the core (e.g., Schwartz 2002). High-redshift sources with such dominant X-ray emission from extended jets have not yet been reported (e.g., Lopez et al. 2006). This IC/CMB enhancement of the X-ray emission could also be observable via noticeable systematic changes with redshift of α_{ox} and the radio-to-X-ray power-law slope,[13] α_{rx}; such increments have not been observed (e.g., Marshall et al. 2005, 2011; Miller et al. 2011).

The potential X-ray absorption in representative high-redshift RLQs is also a critical topic to study. Changes in the strength and frequency of RLQ intrinsic X-ray absorption (i.e., N_H) with redshift have been discussed by many authors (e.g., Elvis et al. 1994a; Cappi et al. 1997; Fiore et al. 1998; Reeves & Turner 2000; Page et al. 2005; Yuan et al. 2006). These studies demonstrate that the fraction of RLQs showing low-energy X-ray cutoffs appears to rise with redshift. These cutoffs are typically attributed to the presence of intrinsic X-ray absorption. Column densities of $N_H \approx (1\text{–}3)\times10^{22}$ cm^{-2} are often seen at $z \gtrsim 2$. RQQs do not show clear evidence for increasing X-ray absorption with redshift; this contrast with RLQs demonstrates that there must be a connection between X-ray absorption and radio loudness. The absorbing gas is thought to be associated with the environments of RLQs, but its precise nature is unclear: it may be circumnuclear, located in the young host galaxy, or entrained by the radio jets. Based on Swift/GRB data set it has also been proposed recently that this absorption may arise in the diffuse intergalactic medium (IGM; e.g., Behar et al. 2011). Three of the seven highly radio-loud ($\log R_L \gtrsim 3$) quasars at $z > 4$ with X-ray spectra show evidence for substantial X-ray absorption (e.g., Fabian et al. 2001; Worsley et al. 2004; Page et al. 2005; Yuan et al. 2006), a finding that is broadly consistent with an extrapolation of the trend observed at lower redshifts. However, the source statistics are limited, and it is precarious to generalize the results from a few extreme highly radio-loud objects to the high-redshift RLQ population as a whole. Note also that moderate low-energy absorption could be mimicked by a curved intrinsic spectrum; this possibility cannot be ruled out for RLQs (e.g., Tavecchio et al. 2007).

In past work, we have targeted representative flat-spectrum RLQs at $z \approx 3.5$–5, typically having moderate R_L values ($R_L \sim 90$–400), using *Chandra* snapshot observations (5–10 ks; Bassett et al. 2004; Lopez et al. 2006). These snapshot observations gave information about the level of X-ray emission and allowed basic population studies. However, they did not allow detailed physical studies of individual objects. Thus, in order to investigate some of the issues described above, we have targeted selected objects from our snapshot samples for longer follow-up observations with *XMM-Newton* and *Chandra*. These observations provide spectral constraints as well as information about long-term X-ray variability. Furthermore, the observations with *Chandra* allow effective searches for kpc-scale X-ray jet emission. We were awarded time to observe four targets with *XMM-Newton* and two targets with *Chandra*. The two targets observed with *Chandra* were selected to follow-up hints of X-ray extension based upon analyses of the snapshot data. We supplemented the follow-up *Chandra* imaging with high-resolution Very Large Array observations to constrain the presence and extent of putative jets.

The layout of this paper is as follows: in Section 2 we describe our sample, the X-ray data reduction, and the radio data reduction; in Section 3 we provide a discussion of the most important results found in this work; and in Section 4 we summarize our results and main conclusions. Throughout this paper, unless stated otherwise, we use cgs units, the errors listed are at the 1σ level, and we adopt a flat Λ-dominated universe with $H_0 = 70$ km s^{-1} Mpc^{-1}, $\Omega_\Lambda = 0.7$, and $\Omega_M = 0.3$.

2. OBSERVATIONS AND DATA REDUCTION

2.1. X-Ray Data

In this work we perform analyses of four new *XMM-Newton* observations and two new *Chandra* observations of high-redshift ($z = 3.6$–5.0) RLQs with moderate R_L. These observations were obtained as a follow-up of *Chandra* snapshot observations (Bassett et al. 2004; Lopez et al. 2006; Shemmer et al. 2006). The original snapshot observations were also reprocessed with the main objective of studying any long-term X-ray variability. The observation logs of the sources analyzed in this work, that include observation dates, observed total counts, total exposure times, and observational identification numbers, are presented in Table 1 for the *XMM-Newton* observations and Table 2 for the *Chandra* observations. Additionally, in Table 3 we present basic optical, X-ray, and radio properties for our sample; among these are the redshift and R_L of each source. The radio-loudness parameters range from ≈90 to 7000 with five out of the six sources having $R_L \lesssim 200$. From Table 3 we also note that our RLQ sample is on average ∼6 times brighter in X-rays than RQQs of similar UV luminosity (based on Just et al. 2007 and Miller et al. 2011). This is suggestive evidence that the X-ray continua of our sample are dominated by jet-linked emission. In Figure 1 we have plotted our sources (with stars) in a diagram of $\log R_L$ versus z. We also have added to this plot RLQs from other high-redshift samples (Page et al. 2005; Shemmer et al. 2005; Yuan et al. 2006; Young et al. 2009) with high-quality X-ray spectra.[14] Our sample is concentrated toward high redshifts and typically representative radio-loudness parameters, where it significantly improves the source statistics. This can be

[13] The radio-to-X-ray power-law slope is defined as $\alpha_{rx} = \log(f_{1\,\mathrm{keV}}/f_r)/\log(\nu_{1\,\mathrm{keV}}/\nu_r)$; in Marshall et al. (2011) the radio frequency used is $\nu_r = 8.64$ GHz.

[14] In the added sample of RLQs there are some sources that have been analyzed in more than one work. The sources with overlap are PMN J0525−3343, RX J1028.6−0844, SDSS J1430+4204 (these three sources were analyzed in Page et al. 2005; Yuan et al. 2006), and SDSS J1510+5702 (analyzed in Page et al. 2005; Yuan et al. 2006; Young et al. 2009). We avoid repeated sources in our extended sample by selecting first the spectral properties of the sources presented in Page et al. (2005), second those presented in Yuan et al. (2006), and third those presented in Young et al. (2009).

Table 1
Log of *XMM-Newton* Observations

Object Name	$\alpha_{2000.0}$[a]	$\delta_{2000.0}$[a]	Obs. Date/ID	Exposure Time[b] (ks)/Total Counts[c]		
				MOS1	MOS2	pn
SDSS J0011+1446	00 11 15.23	+14 46 01.8	2010 Jan 7/0600090101	$29.3(38.5)/761^{+29}_{-28}$	$29.3(38.5)/773^{+29}_{-28}$	$24.5(36.4)/2336^{+49}_{-48}$
PMN J0214−0518	02 14 29.30	−05 17 44.6	2010 Jan 1/0600090401	$58.9(60.5)/186^{+15}_{-14}$	$54.3(60.5)/205^{+15}_{-14}$	$46.0(58.9)/773^{+29}_{-28}$
SDSS J0839+5112	08 39 46.21	+51 12 02.8	2006 Apr 12/0301340101	$9.6(26.6)/101^{+11}_{-10}$	$9.6(26.6)/87^{+10}_{-9}$	$7.4(24.9)/314^{+19}_{-18}$
SDSS J1309+5733	13 09 40.69	+57 33 09.9	2006 Apr 22/0301340501	$29.4(54.6)/85^{+10}_{-9}$	$28.6(54.6)/112^{+12}_{-11}$	$18.3(52.9)/235^{+16}_{-15}$

Notes. Errors on the X-ray counts were computed according to Tables 1 and 2 of Gehrels (1986).
[a] Optical positions in J2000.0 equatorial coordinates. The positions of SDSS J0011+1446 and SDSS J0839+5112 and SDSS J1309+5733 are presented in Adelman-McCarthy et al. (2007), and the position of PMN J0214−0518 is presented in McMahon et al. (2002).
[b] The exposure times and photon counts are obtained after screening the data for flaring. The exposure times before the screening are in parentheses.
[c] Total source counts in a circular region of radius of 30″ centered on the X-ray source. For the MOS cameras and pn camera the photon energies in consideration are the 0.5–10 keV and the 0.3–10 keV observed band, respectively.

Table 2
Log of *Chandra* Observations

Object Name	$\alpha_{2000.0}$[a]	$\delta_{2000.0}$[a]	Obs. Date/ID	Exposure Time[b] (ks)	Total Counts[b,c]	Ref.[d]
New observations						
PMN J0235−1805	02 35 02.50	−18 05 51.0	2009 Feb 22/10306	19.9(21.5)	141^{+13}_{-12}	1
PMN J2219−2719	22 19 35.32	−27 19 03.3	2009 Sep 12/10305	37.9(38.5)	1803^{+43}_{-42}	1
Archival observations						
SDSS J0011+1446	00 11 15.23	+14 46 01.8	2003 May 20/3957	3.5(3.8)	135^{+13}_{-12}	2
PMN J0214−0518	02 14 29.30	−05 17 44.6	2003 Nov 26/4767	4.0(4.3)	44^{+8}_{-7}	3
PMN J0235−1805	02 35 02.50	−18 05 51.0	2004 Feb 7/4766	3.9(3.9)	20 ± 5	3
SDSS J0839+5112	08 39 46.21	+51 12 02.8	2003 Jan 23/3562	4.9(5.0)	82^{+10}_{-9}	4
SDSS J1309+5733	13 09 40.69	+57 33 09.9	2003 Jul 12/3564	4.6(4.7)	31^{+7}_{-6}	4
PMN J2219−2719	22 19 35.32	−27 19 03.3	2003 Nov 19/4769	8.1(8.2)	226^{+16}_{-15}	3

Notes. Errors on the X-ray counts were computed according to Tables 1 and 2 of Gehrels (1986).
[a] Optical positions in J2000.0 equatorial coordinates. The positions of PMN J0235−1805 and PMN J2219−2719 are presented in McMahon et al. (2002).
[b] The exposure times and photon counts are obtained after the screening of the data. The exposure times before the screening are in parenthesis.
[c] Total source counts with energies in the 0.5–8 keV observed band in a circular region of radius of 3.9 arcsec (8 pixels) centered on the X-ray source.
[d] References: (1) This work; (2) Shemmer et al. 2006; (3) Lopez et al. 2006; (4) Bassett et al. 2004.

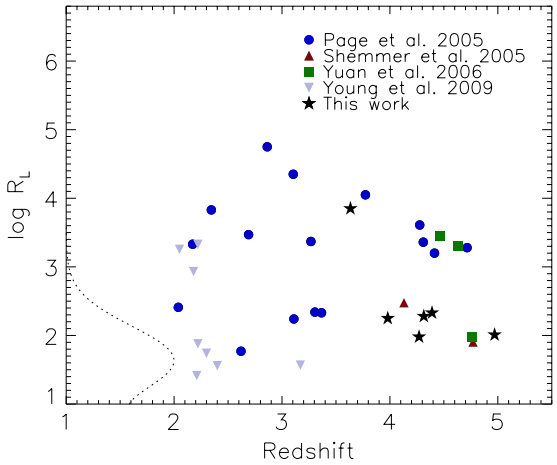

Figure 1. Radio-loudness parameter vs. redshift for our sample (stars) and $z > 2$ RLQs observed with *Chandra* and *XMM-Newton* (circles are from Page et al. 2005, triangles from Shemmer et al. 2005, squares from Yuan et al. 2006, and inverted triangles from Young et al. 2009). The dotted curve along the left side of the plot shows the relative number of RLQs vs. R_L from Ivezić et al. (2002). Note that our sample significantly improves the source statistics for moderately radio-loud quasars at the highest redshifts.

(A color version of this figure is available in the online journal.)

seen from Figure 1 by comparing the R_L of our sources to the R_L distribution found from SDSS/FIRST detections by (Ivezić et al. 2002; dotted-line curve).

The *XMM-Newton* data were analyzed with the Science Analysis Software (SAS) version 10.0.0 provided by the *XMM-Newton* Science Operations Centre (SOC). The event files were obtained by including the events with flag = 0, pattern $\leqslant$ 12 (pattern $\leqslant$ 4), and 200 $\leqslant$ pulse invariant (PI) $\leqslant$ 12,000 (150 $\leqslant$ PI $\leqslant$ 15,000) for the MOS (pn) detectors. The event files were also temporally filtered in order to remove periods of flaring activity.[15] This flaring activity tends to saturate the instrumental background and therefore reduces the good-time intervals. The flaring is especially strong in the observations of SDSS J0839+5112 and SDSS J1309+5733, where the effective observation time has been reduced by 40% and 50%, respectively, when compared with the original exposure time (see Table 1). For the three EPIC detectors (MOS1, MOS2, and pn), the source and background spectra of each quasar were extracted from a circular region with an

[15] To filter the event files of periods of flaring activity, we create light curves using single events with energy greater than 10 keV. Using these light curves we find and remove from the event files the time periods where the count rate is above ∼0.5 count s^{-1} for the MOS cameras and ∼1 count s^{-1} for the pn camera.

Table 3
Optical, X-Ray, and Radio Properties of Surveyed Radio-loud Quasars at High Redshift

Object Name	z	AB_{1450}[a]	$S_{1.4\,GHz}$[b] (mJy)	α_r[c]	α_{ox}[d]	log R_L[e]	log $L_{5\,GHz}$[f]	log L_{2500}[g]	log $L_{2\,keV}$[h]	Δlog $L_{2\,keV}$[i]
SDSS J0011+1446	4.97	18.1	36	−0.12	-1.31 ± 0.03	2.01	34.21	32.08	28.66	1.10
PMN J0214−0518	3.99	18.8	41	+0.65	-1.53 ± 0.04	2.25	34.01	31.65	27.67	0.41
PMN J0235−1805	4.31	18.9	36	+0.26	-1.50 ± 0.04	2.28	34.05	31.64	27.74	0.49
SDSS J0839+5112	4.39	18.8	43	+0.14	-1.40 ± 0.03	2.33	34.16	31.71	28.07	0.77
SDSS J1309+5733	4.27	19.3	11	···	-1.51 ± 0.03	1.98	33.58	31.48	27.53	0.39
PMN J2219−2719	3.63	20.3	304	−0.26	-1.09 ± 0.03	3.85	34.93	30.96	28.11	1.34

Notes.
[a] The monochromatic AB magnitude at rest-frame wavelength 1450 Å. For PMN J0214−0518, PMN J0235−1805, and PMN J2219−2719 we used the R magnitudes found in Hook et al. (2002) to calculate AB_{1450} by using the empirical relation $AB_{1450} = R - 0.684z + 3.10$. For SDSS J0011+1446, SDSS J0839+5112, and SDSS J1309+5733 we used the i-band SDSS magnitudes to calculate AB_{1450} by using the empirical relation $AB_{1450} = i - 0.2$. Note that these estimates of AB_{1450} are reliable within ≈ 0.1–0.2 mag for the redshifts of our sources.
[b] The 1.4 GHz flux density; from the NRAO VLA Sky Survey (NVSS; Condon et al. 1998). For sources covered by VLA FIRST Sky survey (White et al. 1997), their 1.4 GHz flux density differ in less than 10% with the values presented.
[c] The radio power-law slope between 1.4 and 5 GHz (observed frame). The 5 GHz flux density is from the Green Bank 6 cm (GB6; Gregory et al. 1996) or Parkes–MIT–NRAO (PMN; Griffith & Wright 1993) surveys.
[d] The optical-to-X-ray power-law slope $\alpha_{ox} = \log(f_{2\,keV}/f_{2500\,Å})/\log(\nu_{2\,keV}/\nu_{2500\,Å})$. The average difference between measured and predicted α_{ox} for RQQ is $\langle\Delta\alpha_{ox}\rangle \approx 0.3$, based on Steffen et al. (2006) α_{ox}–$L_{2500\,Å}$ relation.
[e] Radio-loudness parameter, defined as $R_L = f_{5\,GHz}/f_{4400\,Å}$ (rest frame; Kellermann et al. 1989). The flux densities at 5 GHz in the rest frame were obtained from the flux densities at 1.4 GHz in the observed-frame assuming a power-law spectrum with spectral slope given by α_r; when α_r is not available we assume $\alpha_r = 0$. The fluxes at 4400 Å in the rest frame are obtained from the AB magnitudes assuming a power-law spectrum with spectral slope of −0.5 (Vanden Berk et al. 2001).
[f] Logarithm of the monochromatic luminosity at 5 GHz. The luminosities were obtained from the flux densities at 1.4 GHz in the observed-frame assuming a power-law spectrum with spectral slope given by α_r; when α_r is not available we assume $\alpha_r = 0$.
[g] Logarithm of the monochromatic luminosity at 2500 Å. These were computed from the AB_{1450} assuming and optical power law of $\alpha = -0.5$ (Vanden Berk et al. 2001).
[h] Logarithm of the absorption-corrected monochromatic luminosity at 2 keV.
[i] The difference between measured and the predicted log $L_{2\,keV}$ for RQQs; based on the Just et al. (2007) relation log $L_{2\,keV} = 0.709 \times \log L_{2500} + 4.822$.

aperture radius of 30″[16] and an annular source-free region with a 50″ inner radius and 100″ outer radius, respectively. The numbers of counts in the source regions for the *XMM-Newton* cameras are presented in Table 1. These counts are selected at energies of 0.5–10 keV for the MOS cameras and 0.3–10 keV for the pn camera. The combined numbers of counts in the EPIC cameras range approximately from 500 to 4000 counts. The response files used to analyze the source spectra were created with the SAS tasks RMFGEN for the redistribution matrix files (RMFs) and ARFGEN for the ancillary response files (ARFs).

The *Chandra* observations (new and archival) were analyzed using the standard software CIAO 4.2 provided by the *Chandra* X-ray Center (CXC). The telemetry format used was Faint mode for all the observations with the exception of obsID 10306 for which Very Faint mode[17] was used. Standard CXC threads were employed to screen the data for status, grade (*ASCA* grade 0, 2, 3, 4, and 6 events), and time intervals of acceptable aspect solution and background levels, only. The source and background spectra of each quasar were extracted (using the CIAO task DMEXTRACT) from a circular region with an aperture radius of 3.″9[18] (8 pixels) and an annular source-free region with an inner radius of 4.″9 (10 pixels) and an outer radius of 39″ (80 pixels), respectively. The numbers of counts in the source regions at energies of 0.5–8 keV are presented in Table 2. The 0.5–8 keV source counts in the new *Chandra* observations of PMN J0235−1805 and PMN J2219−2719 are approximately 140 and 1800 counts, respectively (see Table 2). The 0.5–8 keV source counts in the archival observations range from ≈20 to 230 counts (see Table 2). The response files used to analyze the source spectra were created with the CIAO tasks MKACISRMF for the RMFs and MKARF for the ARFs.

2.2. Radio Data for PMN J0235−1805 and PMN J2219−2719

The two new *Chandra*-observed targets, PMN J0235−1805 and PMN J2219−2719, were observed at the NRAO Very Large Array (VLA) in A configuration, for a nominal resolution of 1.″0 and 0.″39 at 1.4 and 4.9 GHz, respectively. PMN J0235−1805 was observed in 2007 August (observation proposal code AL696), with 100 minutes spent at 1.4 GHz and 28 minutes at 4.9 GHz. PMN J2219−2719 was observed on 2004 October 16 (observation proposal code AC755), for 35 minutes at 1.4 GHz and 12 minutes at 4.9 GHz. Observations were obtained in VLA continuum mode, with two intermediate frequencies and full polarization, for a total bandwidth of 86 MHz. The data were calibrated using the absolute flux-density calibrators 3C48 and 3C147 and the secondary calibrators 0240−231 and 2248−325. Data editing and calibration were carried out in the Astronomical Image Processing System (AIPS). The quasars were imaged using uniform weighting for maximal resolution, and were self-calibrated with a phase-only solution interval of 10 s and amplitude solution intervals of 5 minutes. The VLA synthesized beam at 1.4 GHz and 4.9 GHz at the position of PMN J0235−1805 has dimensions of 2.″04 × 1.″03 at PA = −20.°2 and 0.″55 × 0.″30 at PA = −7.°7, respectively. The VLA synthesized beam at 1.4 GHz and 4.9 GHz at the position of PMN J2219−2719 has dimensions of 2.″70 × 1.″00 at PA = 3.°8 and 0.″80 × 0.″32 at PA = 7.°5, respectively.

[16] The 1.5 keV encircled energy at 30″ from the center of a point source is between 80% and 90% for the EPIC cameras. Note that throughout this work we have applied an aperture correction factor when we calculate fluxes or luminosities.
[17] Very Faint mode offers the advantage of reduced background after ground processing.
[18] The 1.5 keV encircled energy at 3.″9 from the center of a point source is ∼99% for ACIS-S.

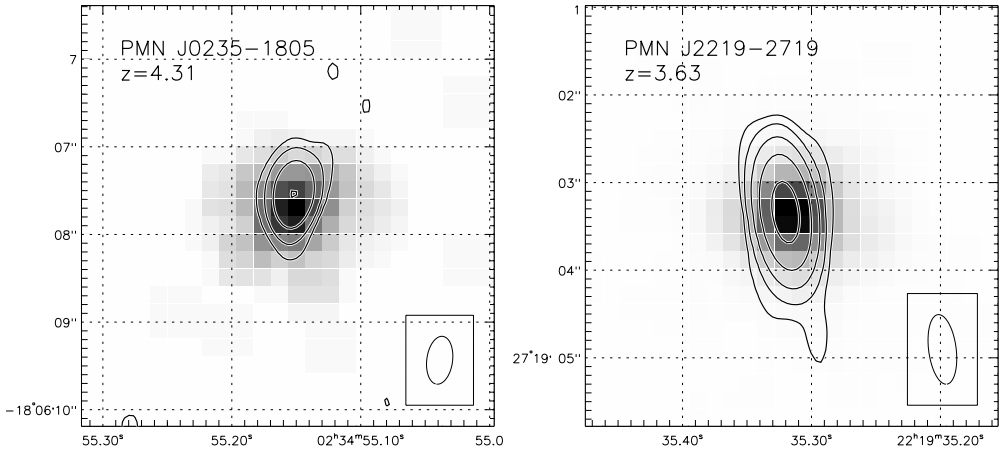

Figure 2. Full band (0.5–8 keV) *Chandra* images of PMN J0235−1805 (left panel) and PMN J2219−2719 (right panel). Each panel spans 4.″4 × 4.″4 on the sky; north is up and east is to the left. Additionally, in each panel the VLA contour plots at 4.9 GHz are shown. The image resolutions of the radio contour plots are 0.″55 × 0.″30 at P.A. = −7.°7 and 0.″80 × 0.″32 at P.A. = 7.°5 for PMN J0235−1805 and PMN J2219−2719, respectively. The contour plots begin at 0.4 mJy per beam and increase by factors of four. Note that in each panel there is an offset between the X-ray image and the radio contours of about 0.″2–0.″3; this offset is within the expected astrometric error of *Chandra*. The elliptical restoring beams are plotted in the lower-right inset of each panel.

3. RESULTS AND DISCUSSION

Here we describe and discuss the main results obtained in this work. We start in Section 3.1 by assessing evidence for extended jets in the *Chandra* images. We continue in Section 3.2 by providing the main results from our spectral analyses with *XMM-Newton* and *Chandra*. In Section 3.3 we constrain long- and short-term variability. Finally, in Section 3.4 we perform correlation analyses between several of the parameters that describe our spectral data; in particular we focus on correlations found in low-redshift samples, as e.g., Γ with log R_L and N_H with z.

3.1. Imaging Analysis with Chandra

The outstanding angular resolution of *Chandra* (∼0.″5) allows us to study any jet that has an X-ray spatial extension larger than ∼5 kpc in the RLQ rest frame. The analysis of the snapshot observations of PMN J0235−1805 and PMN J2219−2719 by Lopez et al. (2006) hinted that these two sources might present extended jets in X-rays. The putative jets found by Lopez et al. (2006) were extended (1″–2″) in the western and southwestern direction for PMN J0235−1805 and PMN J2219−2719, respectively. In both sources the X-ray luminosity of the extended emission was found to be ≈3% that of the core (Lopez et al. 2006).

In Figure 2 we present the new full band X-ray (0.5–8.0 keV) images of PMN J0235−1805 and PMN J2219−2719. In this figure we also have overlaid the contour plots of their 4.9 GHz emission based on the VLA data. From a simple inspection of these images we do not find any obvious evidence for highly extended X-ray emission in these sources. To check further for any evidence of extended emission we have compared a radial profile extracted from each of the *Chandra* images using circular annuli with a point-spread function (PSF) calculated with MARX.[19] The images for each source were made using photons in the soft 0.5–2 keV band and the hard 2–8 keV band. These images were obtained by removing pixel randomization and applying the subpixel algorithm of Li et al. (2004). For each source we obtain a MARX simulation assuming a point source with an X-ray spectrum given by the best-fitted absorbed power-law model from the new observations (see Section 3.2).

From the PSF analysis with MARX we found a hint of spatial extension in PMN J2219−2719 along the southwest direction. In Figure 3 the soft band (left panel) and hard band (right panel) radial profiles of PMN J2219−2719 along the southwest direction are presented. The possible X-ray spatial extension is seen in the soft band[20] through a count overdensity in the data with respect to the PSF around 2″ from the centroid of the source. This count overdensity is seen in two data points with significantly higher counts (∼2σ) than those predicted from the PSF (see left panel of Figure 3). To obtain a basic estimate of the level of putative jet emission in PMN J2219−2719 we measure, in the full band (0.5–8 keV), the excess of counts, with respect to a point source, that lie at >1″ from the core. For this purpose the radial profile of the source is compared with a MARX simulation of a point source. Our results indicate that we have 38^{+13}_{-12} (errors from Gehrels 1986) additional counts[21] in the data when compared with the simulated PSF over a circular aperture extending from 1″ to 4″, which implies that the resolved X-ray emission has a count rate in the full band of (2.1 ± 0.7)% that from the core. Such a level of putative X-ray jet emission is consistent with that estimated by Lopez et al. (2006) using the *Chandra* archival observation of PMN J2219−2719. Additionally, our analyses suggest a southwestern X-ray angular extension of 2″ from PMN J2219−2719 (∼14 kpc in the RLQ rest frame), consistent with the possible ∼1″–2″ extension noted by Lopez et al. (2006). The total number of counts that lie at >1″ from the core and that are inside the southwestern semi-circular sector presented in the upper-right inset of Figure 3 is 47^{+8}_{-7} (errors from Gehrels 1986). In the same area the number of expected counts for a point source (from the MARX PSF) is 24. Based on a Poisson distribution with expected mean 24, the null hypothesis of obtaining 47 counts or more is 2.12×10^{-5}. Therefore the extension found in PMN J2219−2719 has a significance of ≈4.1σ. The putative X-ray jet luminosity in the 2–10 keV rest frame of PMN J2219−2719

[19] MARX is a *Chandra* ray-tracing simulator (for details see http://space.mit.edu/CXC/MARX).

[20] The soft band rest-frame coverage for PMN J2219−2719 is ≈2–9 keV.

[21] For the new *Chandra* observation of PMN J2219−2719 the total number of counts in a circular aperture extending from 1″ to 4″ is 140^{+13}_{-12}, and the number of counts predicted by our PSF simulation is 102.

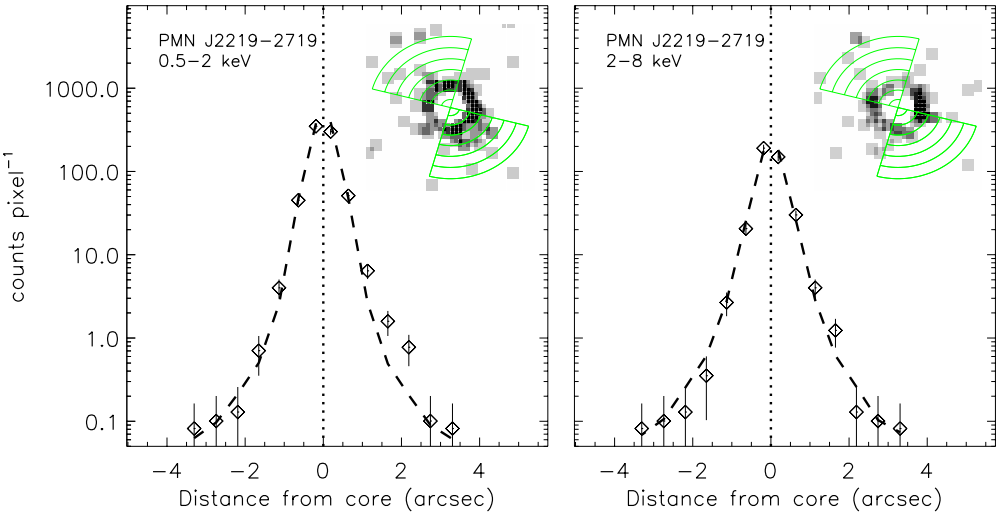

Figure 3. 0.5–2 keV (left panel) and 2–8 keV (right panel) radial profiles of the PMN J2219−2719 core region, constructed from circular sectors shown in the upper-right inset of each panel. The radial profiles are obtained assuming positive distance in the southwestern direction. For presentation purposes, in the upper-right inset of each panel, we have masked the photons coming from a 1 arcsec radius circular region centered at the centroid of the source. The dashed curve shows a scaled PSF generated with MARX with energies close to the average energy of the photons encircled at 2″ from the centroid of the X-ray image.

(A color version of this figure is available in the online journal.)

is log $L_{2-10} \sim 44.6$ (∼2% of the total L_{2-10} luminosity of PMN J2219−2719; see Section 3.2). Given this high X-ray luminosity, the extended emission for PMN J2219−2719 is unlikely to have a non-AGN origin; e.g., starburst activity is typically fainter than log $L_{2-10} \sim 42.5$ (see, e.g., Bauer et al. 2004).

We find a low-level secondary radial structure in the 4.9 GHz image, which can be seen in the southwestern tip of the contour plots in the right panel of Figure 2. This structure is apparent more clearly when we super-resolve the image using a restoring beam of 0.″6 × 0.″6 (see the contour plot in Figure 4). The southwestern extension at 4.9 GHz has a peak flux density of 0.54 mJy per beam, around five times higher than the rms of 0.11 mJy per beam. This 4.9 GHz extension in PMN J2219−2719 is spatially distinct from the southernly extension claimed at 1.4 GHz by Cheung et al. (2006, 2008). At this southernly declination, the VLA synthesized beam at 1.4 GHz has dimensions of 2.″70 × 1.″00, with the major axis oriented north–south. Cheung et al. use a restoring beam of 0.″75 × 0.″75 to deconvolve this source, super-resolving the major axis by almost a factor of four. The claimed secondary radio component extends to the south, in the direction of maximum super-resolution and highest uncertainty. We have similarly super-resolved the 1.4 GHz image of PMN J2219−2719 and are unable to replicate the component shown by Cheung et al. (2006, 2008). To compare agreement between the X-ray extension and the secondary radio structure found at 4.9 GHz in PMN J2219−2719, we performed a maximum likelihood reconstruction (see Section 2.1 of Townsley et al. 2006) on the full band image (250 iterations). The reconstructed image shows various marginal features (1%–3% of the core intensity) at all position angles, although somewhat stronger to the south and west. In Figure 4 we show a reconstructed image (yellow–red–blue indicate decreasing order of count density) with logarithmic intensity scaling. From Figure 4 we note that the X-ray extended emission of PMN J2219−2719 approximately matches the weak radio extension in the southwestern direction.

Additionally, for the new *Chandra* observation of PMN J0235−1805, the excess of X-ray counts that lie at >1″ from the core were consistent with zero when compared with the

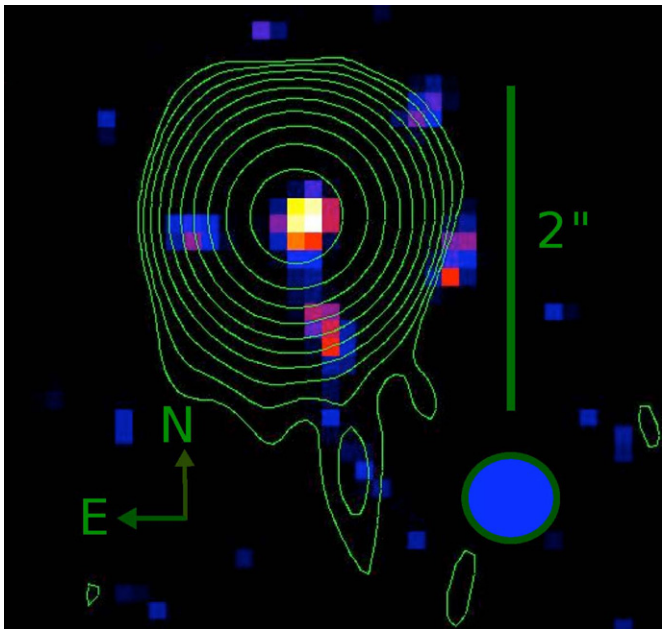

Figure 4. Maximum likelihood reconstruction (see Section 2.1 of Townsley et al. 2006) of the full band X-ray image of PMN J2219−2719. The colors yellow–red–blue indicate the decreasing order of photon count densities. Additionally, a super-resolved VLA contour plot at 4.9 GHz is overlaid. The image resolution of the radio contour plot is 0.″6 × 0.″6. The restoring beam is the blue circle plotted at the lower-right corner. The contours begin at 0.2 mJy per beam and increase by factors of two.

(A color version of this figure is available in the online journal.)

MARX PSF. The line-of-sight projected jet emission in PMN J0235−1805 and PMN J2219−2719 is $\lesssim$2.6% of the core emission in these sources. Similarly, previous work on the $z = 4.30$ RLQ GB 1508 + 5714 demonstrated that the jet-to-core X-ray flux ratio was ∼3% (Siemiginowska et al. 2003; Yuan et al. 2003). The jet X-ray emission in PMN J2219−2719 is also consistent with a mean of ≈4% ($\sigma \approx 6\%$) jet-to-core X-ray flux ratio found in a sample (20 objects) of $z \lesssim 2.6$ quasar jets by Marshall et al. (2005, 2011). Therefore in neither

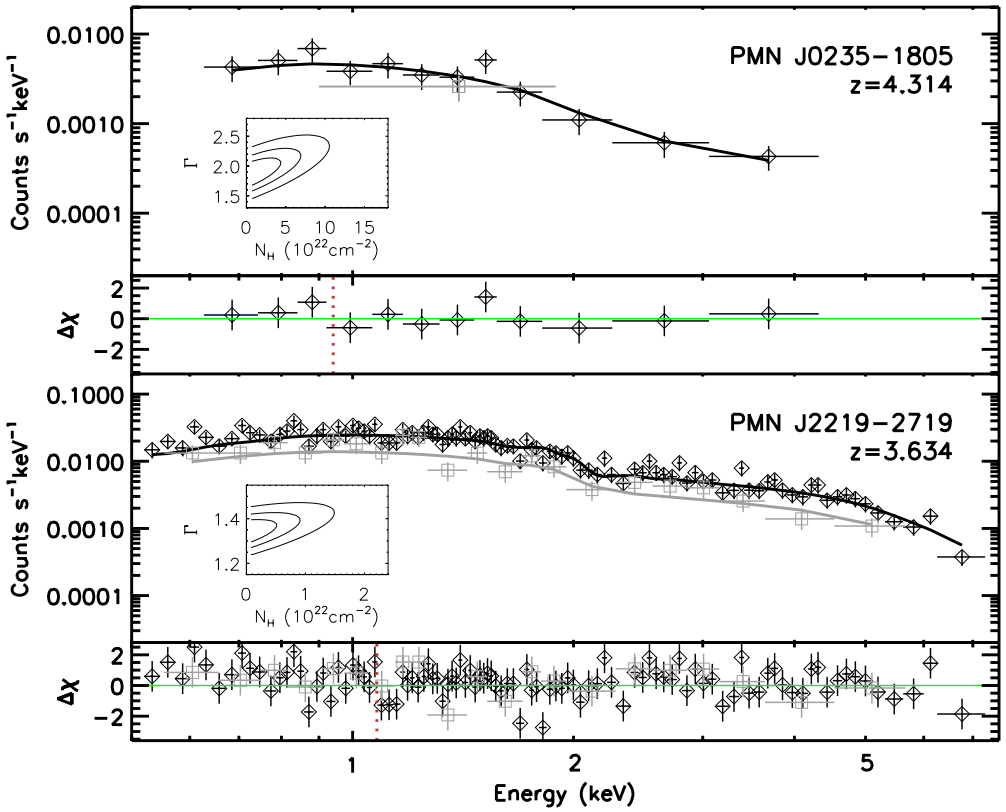

Figure 5. X-ray spectral fits of a power law with Galactic absorption to the *Chandra* observations of PMN J0235−1805 and PMN J2219−2719. The best-fit power law to the data above 5 keV rest frame and extrapolated downward (solid line) is shown. The open diamonds correspond to the data points of our most recent *Chandra* observations of PMN J0235−1805 and PMN J2219−2719. The open squares correspond to the data points of the *Chandra* observations of PMN J0235−1805 and PMN J2219−2719 analyzed in Lopez et al. (2006). The $\Delta\chi$ residuals show the deviation of the data from the model in units of σ with error bars of size unity. In each residual panel we have marked with a dotted vertical line the 5 keV rest-frame energy. The inset in each panel shows 68%, 90%, and 99% confidence contours for the intrinsic absorption ($N_{\rm H}$) and photon index (Γ) using the simultaneous *C*-statistic fits of observations 4766 and 10306 for PMN J0235−1805 and 4769 and 10305 for PMN J2219−2719.

(A color version of this figure is available in the online journal.)

of our new *Chandra* observations do we detect a fractionally large jet emission when compared to the core emission. As a consequence, we do not find any evidence of enhanced jet emission at the high redshifts of these sources as we might expect from the IC/CMB model (see, e.g., Schwartz 2002).

3.2. Spectral Analysis

The spectral analysis was performed using XSPEC v.12.0; the fitting bands used were 0.5–8 keV for the *Chandra* observations, 0.5–10 keV for the *XMM-Newton* MOS camera observations, and 0.3–10 keV for the *XMM-Newton* pn camera observations. For *Chandra* we performed fits for each of the new and archival observations. Since the sources PMN J0235−1805 and PMN J2219−2719 have both new and archival observations with *Chandra*, we have performed a joint spectral fitting of each new observation with its respective archival observation. For these joint fits all the spectral parameters excluding the normalization are constrained to be the same. For the *XMM-Newton* data we performed fits on each of the EPIC camera spectra separately; we also performed joint fits using the three EPIC cameras. The fits for each EPIC camera separately are consistent with the joint fits, and therefore we present only the joint fits in this work.

One of the objectives of the spectral analysis is to determine if intrinsic absorption is important in typical high-redshift RLQs. As a first approach to assess the presence of absorption in our sources, we group the spectra to have between 10 and 30 counts per bin in each observation/instrument. Using these grouped data we fit the observations (using the χ^2 statistic) above 5 keV in the rest frame (about 1 keV in the observed frame) with a power law and then extrapolate it to lower energies. Through the use of this method, the residuals found at low energies may indicate absorption in the spectra. Evidence for absorption is only seen in the spectrum of SDSS J0011+1446 (see Figures 5 and 6). The qualitative analysis above is also consistent with our spectral fits. These spectral fits were performed in the full fitting band of each instrument using the *C*-statistic (Cash 1979).[22] We first try a fit using a power-law model with Galactic absorption and intrinsic absorption (the XSPEC model PHABS*ZPHABS*POW). The Galactic absorption column densities were obtained from Dickey & Lockman (1990); the errors on the Galactic column densities range between $(1\text{and}3)\times10^{19}$ cm^{-2} (Elvis et al. 1994b; Murphy et al. 1996). In all the fits solar abundances were assumed for the Galactic and intrinsic absorption. We do not find evidence of significant intrinsic absorption in five out of our six new RLQ observations. This can be inferred from the best-fitted parameters obtained from the absorbed power-law model. The column densities for these five sources are consistent with zero. Additionally, contour plots of Γ versus $N_{\rm H}$ indicate that a null intrinsic column density is inside the 68% confidence region (see Figures 5 and 6). The source that shows evidence

[22] No spectral grouping was used for the *C*-statistic fits.

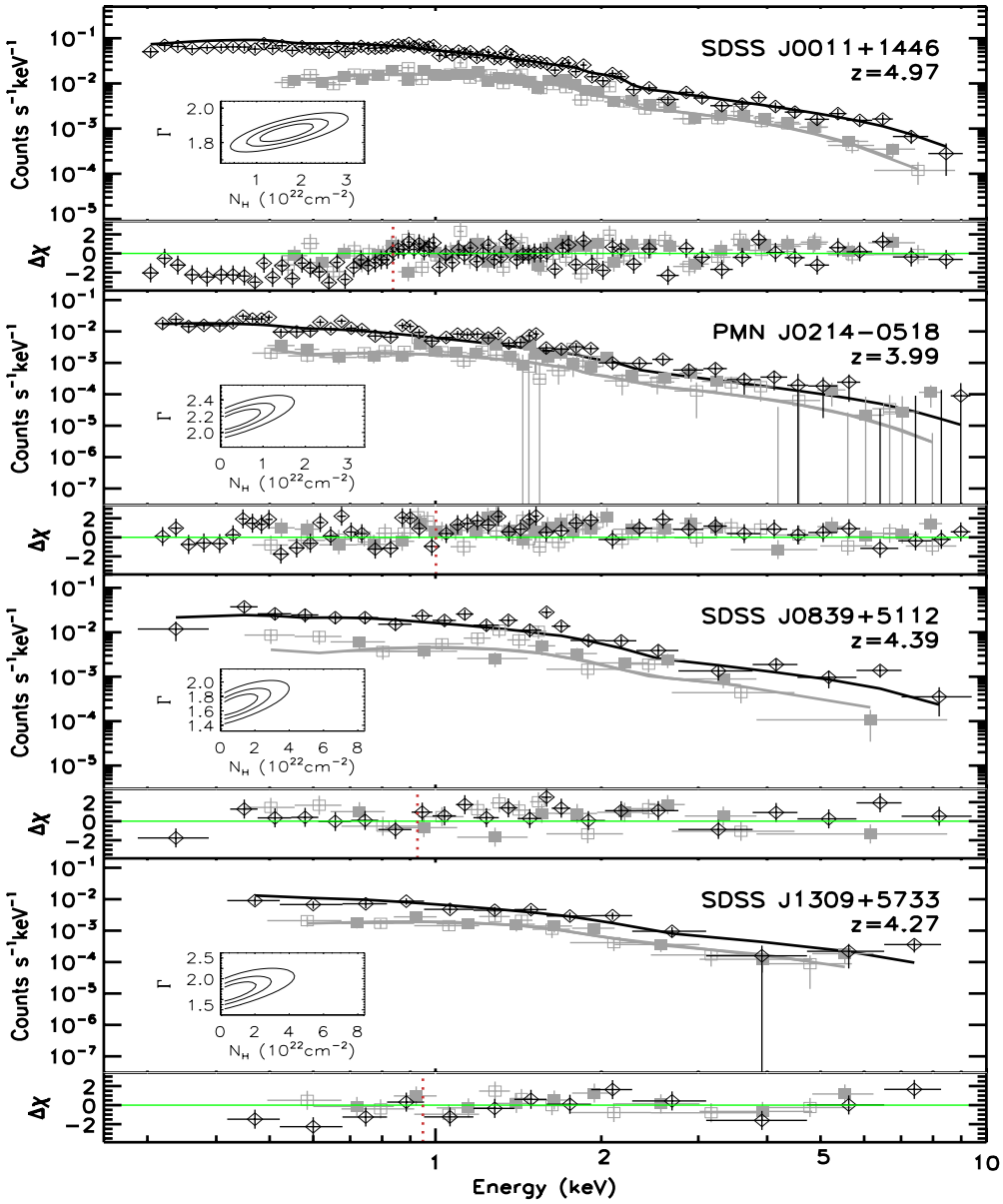

Figure 6. X-ray spectral fits of a power law with Galactic absorption to our new *XMM-Newton* observations of $z \gtrsim 4$ RLQs. The best-fit power law to the data above 5 keV rest frame and extrapolated downward in energy (solid line) is shown. The $\Delta\chi$ residuals show the deviation of the data from the model in units of σ with error bars of size unity. The open diamonds, open squares, and filled squares correspond to the data points of the PN, MOS1, and MOS2 spectra, respectively, for our *XMM-Newton* observations. In each residual panel we have marked with a dotted vertical line the 5 keV rest-frame energy. Note the systematic negative residuals below ≈0.8 keV for SDSS J0011+1446, corresponding to the detected intrinsic absorption. The inset in each panel shows 68%, 90%, and 99% confidence contours for the intrinsic absorption ($N_{\rm H}$) and photon index (Γ) using the simultaneous *C*-statistic fits of the pn, MOS1, and MOS2 data points.

(A color version of this figure is available in the online journal.)

for absorption at >99% confidence is SDSS J0011+1446. The absorption found in this source is of moderate strength ($N_{\rm H} \approx 1.7 \times 10^{22}\,{\rm cm}^{-2}$), in agreement with the absorption found in other high-redshift RLQs (e.g., Page et al. 2005; Yuan et al. 2006). To verify that the absorption detected cannot be reproduced by unaccounted uncertainties in the Galactic absorption, we have fitted the *XMM-Newton* spectra (joint fit of the EPIC cameras) of SDSS J0011+1446 using a Galactic-absorbed power-law model (i.e., the XSPEC model PHABS*POW). The best-fitted absorption obtained, with the absorption at $z = 0$ as a free parameter, is $(7.7 \pm 1.5) \times 10^{20}$ cm^{-2} (error at the 90% confidence level), well above the expected value for Galactic absorption (see Table 4). Based on the fact that just one observation presents absorption, we refit all the other observations (new and archival) with a power-law model with only Galactic absorption (the XSPEC model PHABS*POW). The best-fit spectral parameters (errors and upper limits at the 90% confidence level) are presented in Table 4. In this table, the best-fit photon index and *C*-statistic, of all the observations that do not present absorption, are obtained from a model consisting of a Galactic-absorbed power law. In the case of SDSS J0011+1446 the best-fit photon index and *C*-statistic presented in Table 4 are obtained from a model consisting of a Galactic-absorbed power law with intrinsic absorption at the redshift of the source. The mean photon index for our sample is 1.74 ± 0.11 (1σ error on the mean), in agreement with samples of low-redshift RLQs (Sambruna et al. 1999; Reeves & Turner 2000). Based on this, in Table 4 for the *Chandra* archival observations of PMN

Table 4
Best-fit X-Ray Spectral Parameters

Object Name	ObsID	Galactic N_H[a] (10^{20} cm^{-2})	N_H[b] (10^{22} cm^{-2})	Γ	$f_{0.5-2}$[c]	log L_{2-10}[d]	C-stat(DOF)
XMM-Newton observations							
SDSS J0011+1446	0600090101	4.3	$1.71^{+0.67}_{-0.64}$	1.87 ± 0.07	13.74 ± 0.75	46.62 ± 0.02	1146.4(1336)
PMN J0214−0518	0600090401	2.6	$\leqslant 1.05$	2.10 ± 0.10	1.88 ± 0.19	45.55 ± 0.04	887.8(903)
SDSS J0839+5112	0301340101	3.3	$\leqslant 2.33$	1.61 ± 0.12	$4.42^{+0.73}_{-0.54}$	45.99 ± 0.06	407.3(446)
SDSS J1309+5733	0301340501	1.3	$\leqslant 2.21$	$1.69^{+0.15}_{-0.17}$	1.68 ± 0.24	45.53 ± 0.06	478.0(542)
Chandra observations							
SDSS J0011+1446	3957	4.3	$\leqslant 6.1$	1.90 ± 0.26	$12.31^{+3.98}_{-1.79}$	46.58 ± 0.10	109.6(90)
PMN J0214−0518	4767	2.6	$\leqslant 4.0$	$2.16^{+0.53}_{-0.48}$	$3.72^{+1.23}_{-0.87}$	45.85 ± 0.12	24.1(37)
PMN J0235−1805	10306	2.7	$\leqslant 4.3$	1.86 ± 0.25	2.32 ± 0.37	45.71 ± 0.07	85.4(104)
PMN J0235−1805	4766	2.7	$\leqslant 15.7$	1.70	$1.52^{+0.72}_{-0.46}$	45.52 ± 0.16	23.3(18)
PMN J0235−1805	10306 and 4766	2.7	$\leqslant 4.8$	1.84 ± 0.24	...	...	108.7(122)
SDSS J0839+5112	3562	3.3	$\leqslant 3.4$	1.76 ± 0.32	5.04 ± 1.04	46.06 ± 0.09	54.1(71)
SDSS J1309+5733	3564	1.3	$\leqslant 24.7$	1.70	2.43 ± 0.71	45.71 ± 0.13	24.0(26)
PMN J2219−2719	10305	1.4	$\leqslant 0.6$	1.34 ± 0.06	$12.78^{+0.57}_{-0.71}$	46.28 ± 0.02	443.9(508)
PMN J2219−2719	4769	1.4	$\leqslant 3.2$	1.33 ± 0.18	$7.15^{+1.01}_{-0.94}$	46.03 ± 0.06	154.2(159)
PMN J2219−2719	10305 and 4769	1.4	$\leqslant 0.6$	1.34 ± 0.06	...	...	598.1(668)

Notes. The best-fit column density, were obtained from a model consisting of a Galactic-absorbed power law with intrinsic absorption at the redshift of the source; the same model has been used to estimate the best-fit photon index, and C-statistic for the observations of SDSS J0011+1446. The best-fit photon index, and C-statistic of all the other observations were obtained from a model consisting of a Galactic-absorbed power law. Errors and upper limits represent 90% confidence intervals for each value, taking one parameter to be of interest ($\Delta C = 2.71$; e.g., Avni 1976).

[a] Galactic absorption column densities (from Dickey & Lockman 1990), obtained at the optical coordinates of the sources (see Tables 1 and 2) through the use of the HEASARC N_H tool at http://heasarc.gsfc.nasa.gov/cgi-bin/Tools/w3nh/w3nh.pl

[b] Intrinsic column density in units of 10^{22} cm^{-2}.

[c] Absorption-corrected flux in the observed 0.5–2 keV band in units of 10^{-14} erg cm^{-2} s^{-1}. This flux is obtained from the best-fitted parameters of an absorbed power-law fit. Note that the intrinsic absorption is only important for SDSS J0011+1446; for the *XMM-Newton* observation of this source $f_{0.5-2} = (14.16 \pm 0.75) \times 10^{-14}$ erg cm^{-2} s^{-1} when we do not correct for intrinsic absorption.

[d] Logarithm of the absorption-corrected luminosity in the 2–10 keV rest-frame band; the luminosity is in units of erg s^{-1}.

J0235−1805 and SDSS J1309+5733 we have fixed the power-law photon index to $\Gamma = 1.7$ in order to avoid degeneracies associated with the limited numbers of counts ($\lesssim$30; see Table 2) in these observations.

Since the average redshift of our sources is close to four, the rest-frame band of the fitting for each source reaches energies up to ∼50 keV. Therefore, the source spectra are sampling any potential Compton-reflection component which peaks at rest-frame energies of ∼30 keV (e.g., Lightman & White 1988; Magdziarz & Zdziarski 1995). In general we would not expect reflection signatures to be strong in these sources due to likely dilution by the jet-linked X-ray continuum. To check for reflection we fitted our spectra above 5 keV in the rest frame using the PEXRAV model. From these fits, we find that the reflection parameter is consistent with zero in all our observations, and therefore we do not find that reflection is significant in any of our sources. We also used Gaussian line profiles to fit our spectra in the energy range where the Fe Kα line is found (6.4 keV rest frame for neutral iron). Through this procedure we find that the Fe Kα best-fitted equivalent widths (EWs) are consistent with zero for all our observations, and therefore there is no evidence of Fe Kα signatures in our spectra. For the new observation of SDSS J0011+1446, which is the observation of the highest signal-to-noise ratio, we obtain that the EW of Fe Kα is $\lesssim$170 eV. The upper limit on the EW of Fe Kα line for the other sources is less well constrained. The absence of significant Fe Kα emission lines is consistent with what is expected for luminous ($L_X \gtrsim 10^{46}$ erg s^{-1}; Table 4) quasars (e.g., Nandra et al. 1997; Page et al. 2004; Bianchi et al. 2007).

3.3. Short- and Long-term Variability

We searched for rapid variability in the new *XMM-Newton* and *Chandra* observations by applying the Kolmogorov–Smirnov test to the photon arrival times; however, no significant variability was found. Long-term variability was assessed by comparing the fluxes in the 0.5–2 keV band from the archival observations with those of the new observations. Comparing the fluxes in the two observation epochs of each source (Table 4), we find that one-third of our sample (two out of six) show potential variability. The sources which possibly present variability are PMN J0214−0518, and PMN J2219−2719. In order to test the significance of this variability, we calculate for each source the χ^2 statistic where the data points are the fluxes of each observation (with their respective 1σ errors) and the model is a constant flux with the best fit of the two epochs. The χ^2 value provides a statistical test of the null hypothesis that the flux of each epoch is equal to the best-fitted flux of the two epochs. In Table 5 we list the fluxes for each source in the *Chandra* archival observations (epoch 1) and in the new observations (epoch 2). In this table we also have listed the values of χ^2 for our model to test variability. For PMN J0214−0518 and PMN J2219−2719 we reject the null hypothesis with $>$ 99% significance.[23] The rest-frame

[23] We arrive to the same conclusion if we compare the fluxes in the 0.5–8 keV band from the archival observations with those of the new observations.

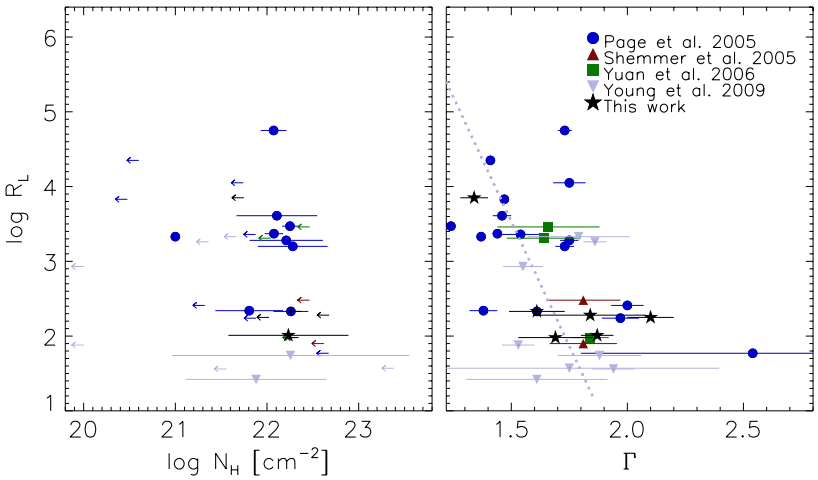

Figure 7. Radio-loudness parameter vs. best-fitted column density (N_H; left panel) and photon index (Γ; right panel) for our sample (stars) and $z > 2.0$ RLQ observations with *Chandra* and *XMM-Newton* (circles are from Page et al. 2005, triangles from Shemmer et al. 2005, squares from Yuan et al. 2006, and inverted triangles from Young et al. 2009). The arrows in the left panel correspond to column density upper limits. The dotted line is obtained by using the IDL Astronomy library tool LINMIX_ERR (Kelly 2007) on our enlarged sample.

(A color version of this figure is available in the online journal.)

Table 5
Two Epoch X-Ray Flux Variability Test

Object Name	$f_{0.5-2}$[a] (epoch 1)	$f_{0.5-2}$[a] (epoch 2)	Δt[b] (days)	χ^2	% sig[c]
SDSS J0011+1446	$12.31^{+2.04}_{-1.09}$	13.74 ± 0.42	406	0.5	51.1
PMN J0214−0518	$3.72^{+0.77}_{-0.52}$	1.88 ± 0.11	446	11.98	>99.9
PMN J0235−1805	$1.52^{+0.46}_{-0.27}$	2.32 ± 0.24	347	2.4	87.8
SDSS J0839+5112	5.04 ± -0.64	$4.42^{+0.47}_{-0.32}$	218	0.6	56.8
SDSS J1309+5733	$2.43^{+0.39}_{-0.47}$	1.68 ± 0.16	193	2.3	87.0
PMN J2219−2719	7.15 ± 0.59	$12.78^{+0.32}_{-0.48}$	459	54.8	>99.9

Notes.
[a] Absorption-corrected flux in the observed 0.5–2 keV band in units of 10^{-14} erg cm^{-2} s^{-1}. For each source the fluxes at epoch 1 and epoch 2 correspond to those obtained from the *Chandra* archival observations and from the new observations (either with *Chandra* or *XMM-Newton*), respectively.
[b] Rest-frame timescale.
[c] Percentile of significance.

Table 6
Correlation Analysis Results for a Combined Sample of High-redshift Radio-loud Quasars

Tested Parameters	Redshift Range	N[a]	r_S[b]	% sig[c]
Γ vs. R_L	$z > 2.0$	35	−0.542	99.9
Γ vs. R_L	$z > 3.0$	22	−0.637	99.9
Γ vs. z	$z > 2.0$	35	0.063	28.1
Γ vs. z	$z > 3.0$	22	0.341	88.0
N_H vs. R_L[d]	$z > 2.0$	35	−0.165	66.4
N_H vs. R_L[d]	$z > 3.0$	22	−0.344	88.5
N_H vs. z[d]	$z > 2.0$	35	0.370	97.0
N_H vs. z[d]	$z > 3.0$	22	0.395	93.0

Notes. The sample used to calculate the correlation parameters corresponds to radio-loud quasars presented in Tables 1 and 2, and those extracted from Page et al. (2005), Shemmer et al. (2005), Yuan et al. (2006), and Young et al. (2009).
[a] Number of RL quasars in each redshift bin.
[b] Spearman correlation coefficient.
[c] Percentile significance of the correlation.
[d] The correlation coefficients involving N_H were calculated using survival analysis with the ASURV code (Isobe et al. 1986).

timescales for the variability are 446 days and 459 days for PMN J0214−0518 and PMN J2219−2719, respectively. The amplitude factors of the flux variability are ≈2.0 and ≈1.8 for PMN J0214−0518 and PMN J2219−2719, respectively; these are in agreement with the typical amplitude factors of lower redshift RLQs (e.g., Brinkmann et al. 1997). The two sources that show evidence for variability are the two with the longest timescales between observations, but this may be merely coincidental.

3.4. Power-law and Absorption Correlation Tests

In order to investigate possible relations between X-ray spectral parameters, redshift, and R_L, we have enlarged our original sample using some of the latest high-redshift ($z > 2$) RLQ X-ray measurements. The R_L versus z diagram of the enlarged sample can be seen in Figure 1 in which the sources from each survey have been indicated with different symbols. We have also plotted in Figure 7 diagrams of R_L versus N_H (left panel) and R_L versus Γ (right panel) for RLQs at $z > 2$. From the right panel we infer a likely decrease of Γ with increasing R_L. To quantify possible dependences between the parameters, we have calculated Spearman correlation coefficients of Γ versus R_L, Γ versus z, N_H versus R_L, and also N_H versus z; the results are given in Table 6 considering sources with $z > 2$ and $z > 3$ separately. We find an anticorrelation between Γ and R_L; this anticorrelation is significant (at the 99.9% confidence level) for RLQs with $z > 2$ and with $z > 3$. The hardening of the spectra with increasing R_L indicates a rising jet contribution to the X-ray spectra as a function of R_L. This conclusion is reinforced by the fact that the excess X-ray luminosity in RLQs (with respect to RQQs) increases with R_L as quantified by, e.g., Miller et al. (2011). Note that, with the exception of PMN J2219−2719, our sources possess moderate values of R_L (see Table 3). The photon index for PMN J2219−2719 of $\Gamma \approx 1.3$ is clearly harder when compared with the photon indices of the other RLQs in our sample (on average ≈1.7; see Section 3.2); this is in agreement with the trend found. Additionally, the soft spectral index ($\Gamma \approx 2.1$) of PMN J0214−0518 ($\log R_L \sim 2$) is also in accordance with the trend found (see Figure 7).

The Pearson correlation coefficient of Γ with $\log R_L$ for our extended sample is −0.487 (significant at the 99.7% confidence level); therefore, as a second step we fit the relation between

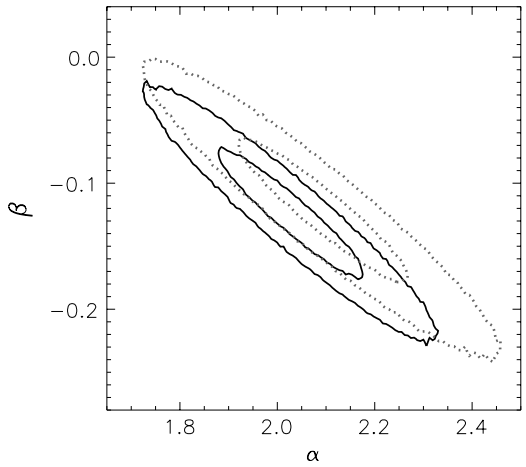

Figure 8. Contour plots of α vs. β for the model $\Gamma = \alpha + \beta \times \log R_L$ using the IDL Astronomy Library tool LINMIX_ERR (Kelly 2007). The solid and dotted contours are the 68% and 99% confidence regions of 2×10^5 realizations for our and the Reeves & Turner data, respectively.

Γ and $\log R_L$ with a simple linear model. This fit is not statistically acceptable because the error bars on Γ are not representative of the intrinsic dispersion of the data around a possible Γ–$\log R_L$ relation. In view of this, we adopt the IDL Astronomy Library tool LINMIX_ERR (Kelly 2007) to estimate the parameters describing a linear model between Γ and $\log R_L$ (i.e., find α and β of $\Gamma = \alpha + \beta \times \log R_L$). This IDL routine, which accounts for measurement errors, nondetections, and intrinsic scatter, is implemented with a Bayesian approach to compute the posterior probability distribution from the observed data. From the random draws (2×10^5 realizations) from the posterior probability distribution we find that the median values of the parameters α and β are given by

$$\Gamma = (2.03 \pm 0.11) + (-0.15 \pm 0.04) \times \log R_L. \quad (1)$$

The Γ–$\log R_L$ relation has already been found in the past in $z \lesssim 2$ samples of RLQs (e.g., Wilkes & Elvis 1987; Reeves & Turner 2000). To test if the relation found in Equation (1) is consistent with that found at lower redshifts, we selected $z < 2$ RLQs from Reeves & Turner (2000). Using LINMIX_ERR (2×10^5 realizations) we find that the median values of the parameters α and β are given by

$$\Gamma = (2.09 \pm 0.16) + (-0.12 \pm 0.05) \times \log R_L. \quad (2)$$

The linear parameters obtained for the $z < 2$ sources of Reeves & Turner (Equation (2)) are consistent with those found for our sources (see Equation (1), and Figure 8); therefore, we do not find evidence that Γ–$\log R_L$ relation changes with redshift.

The correlation tests in Table 6 give indications that $N_{\rm H}$ could be increasing with z for sources with $z > 2$ (in agreement with Reeves & Turner 2000; Page et al. 2005). The correlation of $N_{\rm H}$ with z is at the ∼97% confidence level. Therefore, an apparent correlation between $N_{\rm H}$ and z may be the result of observational bias, since the threshold of absorption that can be measured increases with redshift.[24]

[24] The minimum rest-frame energy of the observed X-ray band increases as (1+z), e.g., for $z \sim 4$ the minimum rest-frame energy of the observed band is $\gtrsim$2 keV. A typical intrinsic absorption of column density $\sim 10^{22}$ cm^{-2} shows a signature in the spectra at rest-frame energies $\lesssim$2 keV. Therefore, the threshold absorption that will produce a significant feature in the spectrum increases with redshift.

4. SUMMARY AND CONCLUSIONS

We have reported the X-ray properties of six high-redshift ($z \gtrsim 4$) RLQs, observed with *XMM-Newton* (four observations) and *Chandra* (two observations) as a follow-up of earlier *Chandra* snapshot observations. A key aspect of our observed sample is that it spans lower values of radio loudness than past studies of high-redshift RLQs in the X-ray regime; the moderate radio-loudness objects studied are much more representative of the overall RLQ population. The main conclusions from our spectral, imaging, and variability analyses are the following.

1. The power-law X-ray continua of our targets have a mean photon index of $\langle\Gamma\rangle = 1.74 \pm 0.11$, consistent with measurements of lower redshift RLQs. They also follow an anticorrelation between photon index and radio loudness seen at lower redshifts. Using linear fits to the Γ–$\log R_L$ relation for an extended sample at $z > 2$, we find consistency of this dependence in relation to lower redshift ($z < 2$) samples. We find no evidence of Compton-reflection continua or iron Kα emission lines. The measured continuum shapes, combined with the fact that our targets are on average ≈6 times brighter in X-rays than RQQs of similar UV luminosity, indicate that jet-linked emission dominates the X-ray continua.
2. We find evidence that one of our targets, SDSS J0011+1446, has significant X-ray absorption with a column density of $N_{\rm H} \approx 1.7 \times 10^{22}$ cm^{-2}. We set useful limits upon X-ray absorption for the rest. The incidence of X-ray absorption in our sample appears roughly consistent with that for more highly radio-loud objects at similar redshifts.
3. In the *Chandra* observation of PMN J2219−2719 we detect a likely X-ray jet with an extension of ∼14 kpc. The X-ray luminosity of this putative jet is ≈2% that of the core. In the *Chandra* observations of PMN J0235−1805 and PMN J2219−2719 we do not find evidence of enhanced extended X-ray jet emission as we might expect from the IC/CMB model. We do not find any evidence of radio extension in the 1.4 and 4.9 GHz VLA images of PMN J0235−1805. We find a secondary structure in the 4.9 GHz VLA image of PMN J2219−2719 that matches the X-ray extension found in this source; due to low resolution we are unable to see this structure in the 1.4 GHz VLA image.
4. Two of our targets, PMN J0214−0518 and PMN J2219−2719, show evidence for X-ray variability by 80%–100% on rest-frame timescales of 450–460 days.

We thank M. Young, B. Kelly, C. C. Cheung, and the anonymous referee for helpful discussions and comments. We acknowledge support from NASA ADP grant NNX10AC99G (CS, WNB), Chandra X-ray Center grant G09-0112X (CS, WNB), and an AAUW American Dissertation Fellowship (LAL). C. Vignali acknowledges support from the Italian Space Agency (ASI) under the ASI-INAF contracts I/009/10/0 and I/088/06/0. B. P. Miller acknowledges support by *Chandra* Award Number GO0-11112A. The National Radio Astronomy Observatory is a facility of the National Science Foundation operated under cooperative agreement by Associated Universities, Inc.

REFERENCES

Adelman-McCarthy, J. K., et al. 2007, ApJS, 172, 634
Avni, Y. 1976, ApJ, 210, 642
Bassett, L. C., Brandt, W. N., Schneider, D. P., Vignali, C., Chartas, G., & Garmire, G. P. 2004, AJ, 128, 523

Bauer, F. E., Alexander, D. M., Brandt, W. N., Schneider, D. P., Treister, E., Hornschemeier, A. E., & Garmire, G. P. 2004, AJ, 128, 2048
Begelman, M. C., Blandford, R. D., & Rees, M. J. 1984, Rev. Mod. Phys., 56, 255
Behar, E., Dado, S., Dar, A., & Laor, A. 2011, ApJ, 734, 26
Bianchi, S., Guainazzi, M., Matt, G., & Fonseca Bonilla, N. 2007, A&A, 467, L19
Brinkmann, W., Yuan, W., & Siebert, J. 1997, A&A, 319, 413
Cappi, M., Matsuoka, M., Comastri, A., Brinkmann, W., Elvis, M., Palumbo, G. G. C., & Vignali, C. 1997, ApJ, 478, 492
Cash, W. 1979, ApJ, 228, 939
Cheung, C. C., Stawarz, Ł., & Siemiginowska, A. 2006, ApJ, 650, 679
Cheung, C. C., Stawarz, Ł., Siemiginowska, A., Harris, D. E., Schwartz, D. A., Wardle, J. F. C., Gobeille, D., & Lee, N. P. 2008, in ASP Conf. Ser. 386, Extragalactic Jets: Theory and Observation from Radio to Gamma Ray, ed. T. A. Rector & D. S. De Young (San Francisco, CA: ASP), 462
Condon, J. J., Cotton, W. D., Greisen, E. W., Yin, Q. F., Perley, R. A., Taylor, G. B., & Broderick, J. J. 1998, AJ, 115, 1693
Dickey, J. M., & Lockman, F. J. 1990, ARA&A, 28, 215
Elvis, M., Fiore, F., Wilkes, B., McDowell, J., & Bechtold, J. 1994a, ApJ, 422, 60
Elvis, M., Lockman, F. J., & Fassnacht, C. 1994b, ApJS, 95, 413
Fabian, A. C., Celotti, A., Iwasawa, K., McMahon, R. G., Carilli, C. L., Brandt, W. N., Ghisellini, G., & Hook, I. M. 2001, MNRAS, 323, 373
Fan, X., Carilli, C. L., & Keating, B. 2006, ARA&A, 44, 415
Fiore, F., Elvis, M., Giommi, P., & Padovani, P. 1998, ApJ, 492, 79
Gehrels, N. 1986, ApJ, 303, 336
Gregory, P. C., Scott, W. K., Douglas, K., & Condon, J. J. 1996, ApJS, 103, 427
Griffith, M. R., & Wright, A. E. 1993, AJ, 105, 1666
Hook, I. M., McMahon, R. G., Shaver, P. A., & Snellen, I. A. G. 2002, A&A, 391, 509
Isobe, T., Feigelson, E. D., & Nelson, P. I. 1986, ApJ, 306, 490
Ivezić, Ž., et al. 2002, AJ, 124, 2364
Jiang, L., Fan, X., Ivezić, Ž., Richards, G. T., Schneider, D. P., Strauss, M. A., & Kelly, B. C. 2007, ApJ, 656, 680
Just, D. W., Brandt, W. N., Shemmer, O., Steffen, A. T., Schneider, D. P., Chartas, G., & Garmire, G. P. 2007, ApJ, 665, 1004
Kellermann, K. I., Sramek, R., Schmidt, M., Shaffer, D. B., & Green, R. 1989, AJ, 98, 1195
Kelly, B. C. 2007, ApJ, 665, 1489
Li, J., Kastner, J. H., Prigozhin, G. Y., Schulz, N. S., Feigelson, E. D., & Getman, K. V. 2004, ApJ, 610, 1204
Lightman, A. P., & White, T. R. 1988, ApJ, 335, 57
Lopez, L. A., Brandt, W. N., Vignali, C., Schneider, D. P., Chartas, G., & Garmire, G. P. 2006, AJ, 131, 1914
Magdziarz, P., & Zdziarski, A. A. 1995, MNRAS, 273, 837
Marshall, H. L., et al. 2005, ApJS, 156, 13
Marshall, H. L., et al. 2011, ApJS, 193, 15
McMahon, R. G., White, R. L., Helfand, D. J., & Becker, R. H. 2002, ApJS, 143, 1
Miller, B. P., Brandt, W. N., Schneider, D. P., Gibson, R. R., Steffen, A. T., & Wu, J. 2011, ApJ, 726, 20
Murphy, E. M., Lockman, F. J., Laor, A., & Elvis, M. 1996, ApJS, 105, 369
Nandra, K., George, I. M., Mushotzky, R. F., Turner, T. J., & Yaqoob, T. 1997, ApJ, 488, L91
Page, K. L., O'Brien, P. T., Reeves, J. N., & Turner, M. J. L. 2004, MNRAS, 347, 316
Page, K. L., Reeves, J. N., O'Brien, P. T., & Turner, M. J. L. 2005, MNRAS, 364, 195
Reeves, J. N., & Turner, M. J. L. 2000, MNRAS, 316, 234
Saez, C., Chartas, G., Brandt, W. N., Lehmer, B. D., Bauer, F. E., Dai, X., & Garmire, G. P. 2008, AJ, 135, 1505
Sambruna, R. M., Eracleous, M., & Mushotzky, R. F. 1999, ApJ, 526, 60
Schwartz, D. A. 2002, ApJ, 569, L23
Shemmer, O., Brandt, W. N., Netzer, H., Maiolino, R., & Kaspi, S. 2008, ApJ, 682, 81
Shemmer, O., Brandt, W. N., Vignali, C., Schneider, D. P., Fan, X., Richards, G. T., & Strauss, M. A. 2005, ApJ, 630, 729
Shemmer, O., et al. 2006, ApJ, 644, 86
Siemiginowska, A., Smith, R. K., Aldcroft, T. L., Schwartz, D. A., Paerels, F., & Petric, A. O. 2003, ApJ, 598, L15
Steffen, A. T., Strateva, I., Brandt, W. N., Alexander, D. M., Koekemoer, A. M., Lehmer, B. D., Schneider, D. P., & Vignali, C. 2006, AJ, 131, 2826
Tananbaum, H., et al. 1979, ApJ, 234, L9
Tavecchio, F., Maraschi, L., Ghisellini, G., Kataoka, J., Foschini, L., Sambruna, R. M., & Tagliaferri, G. 2007, ApJ, 665, 980
Townsley, L. K., Broos, P. S., Feigelson, E. D., Garmire, G. P., & Getman, K. V. 2006, AJ, 131, 2164
Vanden Berk, D. E., et al. 2001, AJ, 122, 549
White, R. L., Becker, R. H., Helfand, D. J., & Gregg, M. D. 1997, ApJ, 475, 479
Wilkes, B. J., & Elvis, M. 1987, ApJ, 323, 243
Worrall, D. M. 2009, A&AR, 17, 1
Worrall, D. M., Tananbaum, H., Giommi, P., & Zamorani, G. 1987, ApJ, 313, 596
Worsley, M. A., Fabian, A. C., Turner, A. K., Celotti, A., & Iwasawa, K. 2004, MNRAS, 350, 207
Young, M., Elvis, M., & Risaliti, G. 2009, ApJS, 183, 17
Yuan, W., Fabian, A. C., Celotti, A., & Jonker, P. G. 2003, MNRAS, 346, L7
Yuan, W., Fabian, A. C., Worsley, M. A., & McMahon, R. G. 2006, MNRAS, 368, 985
Zamorani, G., et al. 1981, ApJ, 245, 357